Article

Opto-twistronic Hall effect in a three-dimensional spiral lattice

https://doi.org/10.1038/s41586-024-07949-1

Received: 7 November 2023

Accepted: 14 August 2024

Published online: 18 September 2024

Check for updates

Zhurun Ji[1,2,3,5], Yuzhou Zhao[4], Yicong Chen[2], Ziyan Zhu[3], Yuhui Wang[1], Wenjing Liu[1,6], Gaurav Modi[1], Eugene J. Mele[2], Song Jin[4] & Ritesh Agarwal[1]✉

Studies of moiré systems have explained the effect of superlattice modulations on their properties, demonstrating new correlated phases[1]. However, most experimental studies have focused on a few layers in two-dimensional systems. Extending twistronics to three dimensions, in which the twist extends into the third dimension, remains underexplored because of the challenges associated with the manual stacking of layers. Here we study three-dimensional twistronics using a self-assembled twisted spiral superlattice of multilayered WS_2. Our findings show an opto-twistronic Hall effect driven by structural chirality and coherence length, modulated by the moiré potential of the spiral superlattice. This is an experimental manifestation of the noncommutative geometry of the system. We observe enhanced light–matter interactions and an altered dependence of the Hall coefficient on photon momentum. Our model suggests contributions from higher-order quantum geometric quantities to this observation, providing opportunities for designing quantum-materials-based optoelectronic lattices with large nonlinearities.

Chiral states of matter, such as one-dimensional helical nanotubes[2] and two-dimensional (2D) moiré systems[3], offer new functionalities. The effect of quantum geometry on their properties as well as the emergence of new phases have gained a lot of interest[4]. Optical studies have also shown new properties associated with the modified lattice geometry in 2D moiré systems[5–10]. However, most of these studies have been limited to few-layer systems, primarily because of the challenges associated with manual stacking of individual layers. Theoretical predictions suggest that increasing the layer numbers could lead to phenomena such as moiré of moiré modulation[11], topological phase transition[12], optical rotation[13] and the emergence of new resonant states[14,15], demonstrating the potential of extending twistronics to three dimensions.

In this context, the transition from 2D to three-dimensional (3D) twistronic systems poses a fundamental question of how would the expanded length scales of moiré lattice and sample thickness alter light–matter interactions as they approach optical wavelengths. The situation becomes complex for systems in which the twist forms a pattern or quasi-periodicity in the third dimension with non-commutative primitive translations. The physics related to noncommutative dynamics is universal with examples ranging from the motion of charged quantum particles in a magnetic field and anomalous velocity. These characteristics suggest that in 3D twistronics, the principles governing light–matter coupling could be largely changed, and these alterations could lead to new responses tied to the underlying quantum geometry[16]. Nonetheless, these hypotheses have not been experimentally tested.

Recent advances in materials growth have led to the discovery of a few 3D spirally stacked systems, including twisted GeS (ref. 17) and supertwisted WS_2 (ref. 18). Notably, the supertwisted spiral of WS_2 is formed by a growth mechanism driven by screw dislocation with tens to hundreds of layers, a nearly uniform twist angle between layers with a nonsymmorphic screw symmetry and the presence of moiré of moiré superlattices[18,19] with large optical nonlinearities[20]. However, the complex geometry of supertwisted lattices presents challenges for experimental investigation; consequently, their properties remain largely unexplored.

To study the properties of twisted 3D spiral lattices, we investigate hexagonal supertwisted WS_2 samples[18,21] (Fig. 1a and Methods) in which the base is 2H stacked WS_2. With the large number of layers in the system and the plethora of high-order moiré patterns of different lengthscales[11] (Fig. 1b), the linear optical spectra (Fig. 1c; discussed later) become congested, thereby limiting the information content. Therefore, we performed nonlinear optical Hall measurements to gain a microscopic understanding of fundamental optical excitations in these 3D spiral systems. We demonstrate an opto-twistronic Hall response driven by the noncommutative geometry of the supertwisted system, demonstrating the interplay between structural, electronic and quantum geometry.

Linear optical characterization of supertwisted WS_2

We investigated the linear optical properties of supertwisted WS_2 at room temperature and observed a distinct intralayer A-exciton reflectance dip at around 636 nm (Fig. 1c), with no discernible differences in the reflectance spectra because of structural chirality when interacting with left and right circular polarization of light, above the detection limit[22] (Fig. 1c and Extended Data Fig. 1). The exciton formation process (Fig. 1d) in supertwisted WS_2 can be modelled with exciton eigenfunctions composed of an in-plane component and a standing wavefunction in the z-direction[23] (Supplementary Note 2.2). It distinguishes itself from

[1]Department of Materials Science and Engineering, University of Pennsylvania, Philadelphia, PA, USA. [2]Department of Physics and Astronomy, University of Pennsylvania, Philadelphia, PA, USA. [3]Stanford Institute for Materials and Energy Sciences, SLAC National Accelerator Laboratory, Menlo Park, CA, USA. [4]Department of Chemistry, University of Wisconsin-Madison, Madison, WI, USA. [5]Present address: Department of Physics and Applied Physics, Stanford University, Stanford, CA, USA. [6]Present address: State Key Laboratory for Mesoscopic Physics and Frontiers Science Center for Nano-optoelectronics, School of Physics, Peking University, Beijing, China. ✉e-mail: riteshag@upenn.edu

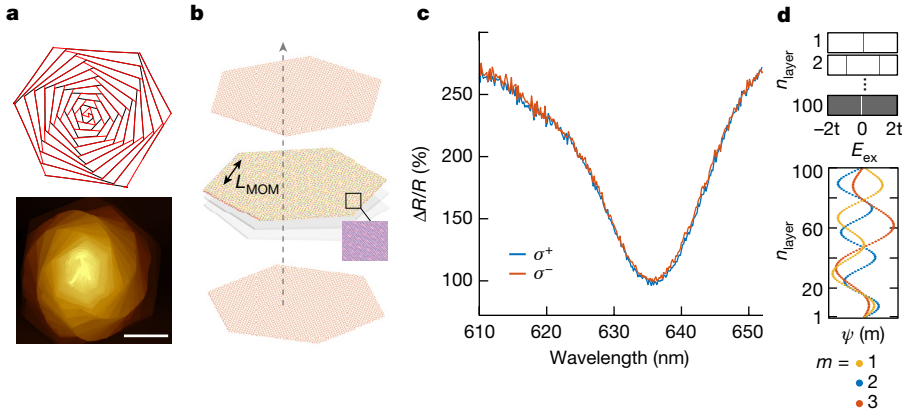

Fig. 1 | Illustration and linear optical characterization of the 3D supertwisted spirals of WS_2. a, Schematic of the supertwisted sample (top) based on hexagonal WS_2 spirals (2H stacking arrangement). AFM image (bottom) of a representative supertwisted WS_2 sample with continuously twisting layers. Scale bar, 4 µm. **b**. Illustration of the moiré of moiré pattern in the supertwisted system. The grey arrow shows the screw rotation axis. L_{MOM} denotes the length of a moiré of moiré unit cell, which can be orders of magnitudes larger than the crystal unit cell and can become comparable to optical wavelengths (about 100 nm). The magnified image shows the moiré pattern formed in the bilayer region with a smaller length scale than that in the multilayers. **c**. Reflectance spectra measured with left and right circularly polarized light. **d**. Illustrations of the exciton eigenenergy distributions (top; in which the distributions for 1-, 2- and 100-layer systems are shown), and layer-hybridized exciton wavefunctions (m = 1–3 in a 100-layer system) in the supertwisted system (bottom).

2H- or 3R-stacked WS_2 (ref. 21), because the lattice twist gives rise to a series of shifted eigenmodes. When the stack becomes thick, the energy separation between the modes becomes smaller than spectral broadening to form a broad dip, as observed. Therefore, the supertwisted samples call for a different probe to explore their properties.

Opto-twistronic Hall effect

We then conducted optical Hall measurements, a nonlinear probe, in which the magnetic field in the conventional Hall effect is replaced by a polarized laser beam and is extremely sensitive to the symmetries of the material[24]. The supertwisted WS_2 flakes were etched into a Hall bar geometry with uniform thickness (Fig. 2a (device D1) and Methods). We optically excited the sample near the exciton resonance and applied an in-plane voltage V_0 to dissociate the charge-neutral excitons. The resulting photovoltage, V_H was measured along the perpendicular in-plane direction as a function of optical polarization (Methods). The laser was incident on the sample at zenith and azimuthal angles of θ and α, respectively, passing through a quarter-wave plate (QWP), with a rotation angle ϕ with respect to its fast axis (Fig. 2b and Extended Data Fig. 2). In device D1, the photovoltage was recorded as a function of QWP angle (laser incident normally on the sample, that is, $\theta = 0°$). The red line (Fig. 2c, middle) shows the part sensitive to the circular polarization of light, or circular Hall photovoltage, V_{HC}, and the blue line (Fig. 2c, bottom) shows the linear polarization-dependent Hall photovoltage, V_{HL}. The results show that Hall photovoltage depends on both linear and circular polarizations (Supplementary Note 2.3). To examine the possible origins of V_{HC}, V_0 was swept while V_{HC} was measured at different excitation wavelengths. The observed linearity of both V_{HC} and longitudinal current I_0 as a function of V_0 (Fig. 2d) shows ohmic contacts[25], with minimal Schottky junction contributions. The zero-voltage offset of V_{HC} indicates the presence of defect-mediated exciton dissociation

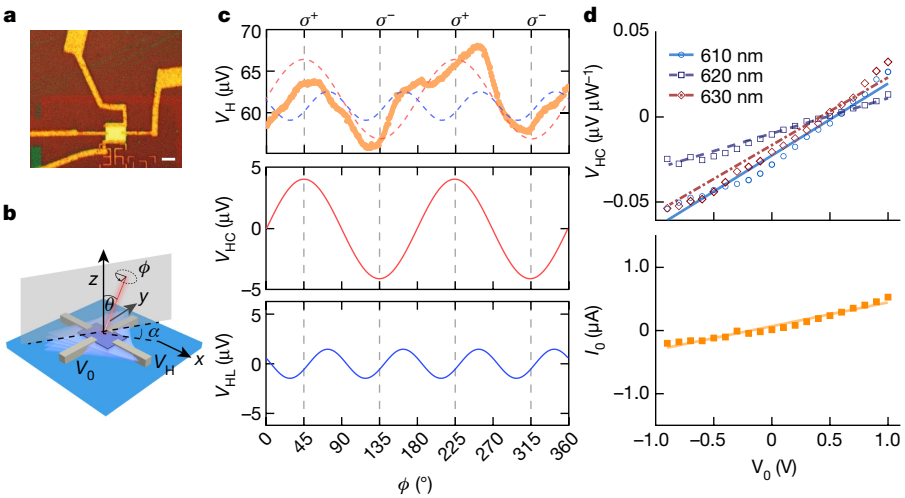

Fig. 2 | Opto-twistronic Hall effect measurements on the supertwisted WS_2 sample. a. Optical image of the Hall bar device (D1) based on the supertwisted WS_2 sample, fabricated with Bi/Cu electrodes. Scale bar, 5 µm. **b**, Schematic of the optoelectronic measurement with incidence zenith angle θ, azimuthal angle α, quarter-wave plate rotation angle ϕ with respect to its fast axis, applied transverse voltage V_0 and measured Hall voltage V_H. **c**. The top panel shows the Hall voltage V_H as a function of ϕ at $V_0 = 1$ V as the set of yellow dots. The red line in the middle panel is a fit for the circular polarization-dependent part of V_H (or V_{HC}). The blue line in the bottom panel is a fit for the linear polarization-dependent part of V_H (or V_{HL}). The two fittings are added to the top panel as dashed lines with an arbitrary offset for illustration. **d**, Measurement of transverse V_{HC} is shown as a function of applied voltage V_0 at three different excitation wavelengths (top), showing an ohmic behaviour. Longitudinal photocurrent I_0 is shown as a function of V_0, also showing an ohmic response (bottom).

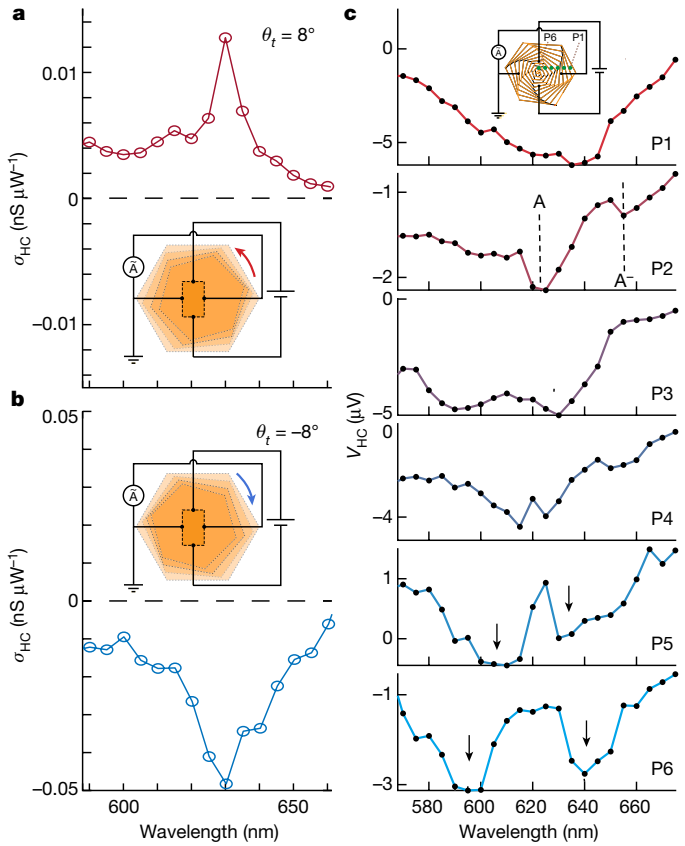

Fig. 3 | Interlinkage between the supertwisted spiral geometry and the opto-twistronic signal. a. The spectrum of Hall conductivity σ_{HC} (C denotes the part dependent on circular polarization) measured on an approximately 8° left-handed supertwisted sample (D2). Inset, schematic of device D2. **b**, The spectrum of Hall conductivity σ_{HC} measured on an approximately −8° right-handed supertwisted sample (D3), showing a sign reversal of the response. Inset, schematic of device D3. **c**, The images from the top to bottom show the V_{HC} wavelength spectra measured at six spots P1–P6 marked on the inset schematics, from the thinnest to the thickest region showing a splitting in the Hall voltage induced by the exciton–photon coupling. Inset, the schematic of sample D4.

in TMDs[26]. Therefore, these results suggest an intrinsic Hall response in the supertwisted system that is sensitive to light chirality. By contrast, V_{HC} vanishes in a similar 2H-stacked multilayer MoS_2 system[27] because of the absence of mechanisms separating the photoexcited electron and hole trajectories. The nonlinear V_{HC} observed in supertwisted systems is distinct from the circular dichroism of twisted bilayers[28–31] and is many orders of magnitude higher (Supplementary Note 2.1). This distinction calls for a deeper exploration of the relationship between the symmetry and geometric properties of the system.

Handedness and thickness dependences

To explore the influence of the handedness of the structural stacking of supertwisted WS_2 on its nonlinear optical response, we measured V_{HC} on a series of samples in the Hall bar geometry (Fig. 3a,b). As V_{HC} vanishes when the interlayer twist angle is 60° (that is, 2H stacking), we selected two supertwisted WS_2 samples to study the optical Hall voltage with supertwisting angle: device D2 with anticlockwise (about +8° twist between the adjacent layers) and device D3 with clockwise (about −8° twist between the layers) twisting from the bottom to the top layer (see Supplementary Note 1.4 and Supplementary Fig. 8 for optical and AFM images). With a similar device geometry and measurement configuration, the optical Hall conductivity σ_{HC} (obtained from the measured photovoltage V_{HC}) shows a sign reversal (Fig. 3a,b), showing that the handedness of the system governs the optical response, further confirming its origin as supertwisting. Therefore, we name the response as opto-twistronic Hall effect.

To describe the opto-twistronic Hall phenomena in the supertwisted system, we model the light field as $E_i(\mathbf{r}, t) = E_i^{i(\mathbf{q}\cdot\mathbf{r}-\omega t)} + \text{c. c.}$ where $\mathbf{q}$ is the photon momentum. The circular-polarization-dependent Hall current $\mathbf{J}(\mathbf{q}, \omega)$ is determined by a nonlinear conductivity tensor $\boldsymbol{\sigma}^{(2)}$ (Methods). For the case of a monolayer WS_2 under bias, $\boldsymbol{\sigma}^{(2)}$ originates from the opposite sign of anomalous velocity in different valleys, that is, the valley Hall effect[27]. In the case of 2H-stacked multilayers, $\boldsymbol{\sigma}^{(2)}$ in each layer is cancelled out by the neighbouring layer because of valley degeneracy[32]. By contrast, carrier dynamics in the supertwisted material can be analysed by considering the free propagation of a particle in a helical frame of reference (see the Methods for the derivation of the Hamiltonian), which becomes completely analogous to the situation for a charged particle moving in a magnetic field with an effective strength, $B^* = \frac{2\hbar\kappa_z\beta}{e}$. However, unlike a physical magnetic field, the effective field B^* is odd in the quasi-momentum κ_z, reflecting the time-reversal symmetry of the twisted structure. Any nonequilibrium state distribution breaking time-reversal symmetry, for example, under excitation with circularly polarized light, will undergo a net transverse deflection in response to an in-plane bias, identifiable by the induced Hall response. Importantly, B^* is odd in β, resulting in the reversal of the Hall field in enantiomeric structures, as observed. We estimate B^* to be approximately 4 T for the supertwisted WS_2 structures with an approximately +8° twist angle.

To explore how the properties of supertwisted WS_2 evolve with thickness, V_{HC} was measured on a thick flake at different thickness regions (locations denoted by green circles on device D4, Fig. 3c inset) at 77 K. In the thinnest region, that is, P1 location in Fig. 3c, the V_{HC} spectrum (that is, laser excitation energy dependence of V_{HC}) shows a prominent peak at the A-exciton wavelength (about 620 nm) and another smaller, redshifted peak associated with the charged exciton absorption (A^-) (ref. 33). The presence of a trion feature indicates that the system contains free charges that bind with excitons, consistent with the conventional *n*-doped behaviour of WS_2. Although the accurate peak assignment is limited by the current experimental accuracy, as the sample thickness increases, the overall trend shows that the V_{HC} peak splits and increases in magnitude. These observations show that the V_{HC} spectrum is far more complex than a simple superposition of responses from different layers. The splitting of the V_{HC} peak with increased thickness is consistent with the stronger light–matter coupling observed in the reflectance spectra of strongly coupled optical cavities[34], but in our measurements, it is seen in V_{HC} data and without external cavities. Angle-resolved reflectance measurements were also conducted to confirm the strong exciton–photon mode coupling[34,35] in the samples (details in Supplementary Note 1.2). These results indicate that exciton–photon coupling can strongly affect the nonlinear optoelectronic response from the layer-hybridized excitons. It also demonstrates that on stacking from 2D to 3D, the system develops another controllable degree of freedom, that is, the number of layers, which has a notable impact on the opto-twistronic Hall effect.

Effect of photon momentum

Both the layer thickness and handedness dependence of the opto-twistronic Hall effect suggest its relationship with the nonsymmorphic symmetry of the supertwisted system. To explore the role of the twist angle between neighbouring layers on the nonlinear optical response, we altered the direction and magnitude of $\mathbf{q}$ (projected onto the supertwisting axis $\hat{z}$) and mapped the changes in V_{HC}. Measurements were carried out on circular-shaped supertwisted WS_2 devices, that is, a symmetric Hall bar geometry (Fig. 4a) at 77 K, in which V_{HC} was measured as a function of the θ_y (incidence zenith angle in the *y*-direction; Fig. 2c) at the A-exciton wavelength (620 nm). Laser

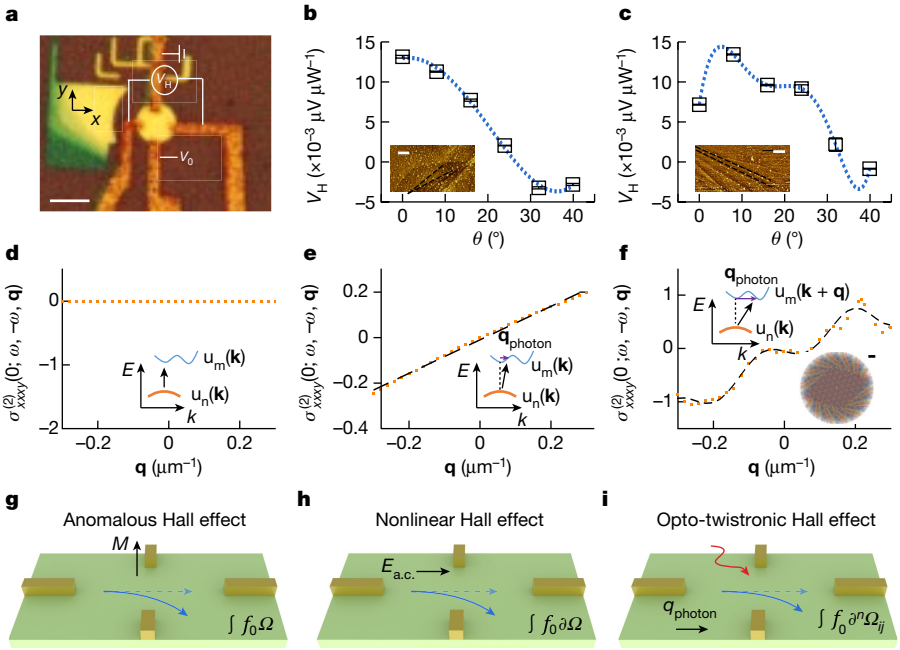

Fig. 4 | Opto-twistronic Hall response from spiral lattice-photon momentum interactions. a. Optical image of the circular Hall bar device D5. Scale bar, 5 μm. **b**. Incidence angle (θ_y) dependence of V_{HC} on sample D6. Data are presented as black squares with error bars (standard deviation calculated from 40 measurements), and the blue dotted line is the fitting summing over different orders of photon momentum **q**. Scale bar, 1 μm. Inset, AFM image of sample D6, showing 15°–20° twist angles. **c**, Incidence angle (θ_y) dependence of V_{HC} on sample D5. Data are presented as black squares with the error bar (standard deviation calculated from 40 measurements), and the blue dotted line is the fitting summing over different orders of photon momentum **q**. Scale bar, 1 um. Inset, the AFM image of D5, showing 1°–5° twist angles. **d**–**f**, A representative second-order optical conductivity tensor element calculated for **d**. Monolayer WS_2 tight binding model; prototypical twisted homobilayer TMD model with a twist angle of 1°; supertwisted TMD model with a continuous twist angle of 2°. Insets in **d**–**f**, schematics showing the corresponding optical excitation processes, where the photon momentum **q** (purple arrow) connects Bloch states of bands n (orange) and m (blue) at different momenta. Yellow dots are calculated $\sigma^{(2)}_{xxy}$ and black dashed lines are the polynomial fittings. Additional inset in **f**, the moiré patterns of a 3.5° supertwisted structure (see Supplementary Fig. 11 for details). Scale bar denotes 10 lattice vectors. **g**–**i**, Schematics showing the anomalous Hall effect (**g**), nonlinear Hall effect (**h**) and the opto-twistronic Hall effect (**i**).

incidence-angle-dependent photogalvanic effect in various systems typically shows a sinusoidal pattern, which shows the dominant matrix elements of photogalvanic conductivity and related sample symmetries[33,36]. The supertwisted WS_2 sample D6 (Supplementary Note 1.4) with large (about −15° to −20°) twist angles between neighbouring layers, shows a sinusoidal dependence of V_{HC} with θ_y (Fig. 4b), similar to monolayer TMDs[33]. On the other hand, sample D5 with similar thickness and geometry but smaller twist angles (<5°; Fig. 4c) shows a strongly non-sinusoidal angle dependence and a smaller V_{HC} (likely related to charge trapping by the moiré potential). This unusual incidence angle dependence of V_{HC} is not a result of sample inhomogeneities, strain or other extrinsic factors (Supplementary Fig. 7). The contrast between the two samples and the absence of measurable circular dichroism (Fig. 1c) further rule out effects due to finite out-of-plane components of the optical field.

The strong non-sinusoidal feature observed for small twist-angle samples implies a complex dependence of V_{HC} on **q** (see fitting in Fig. 4c, which shows contribution from higher orders of photon momentum **q**). This is different from the conventional second-order optical conductivity, that is, $\boldsymbol{\sigma}^{(2)} = \boldsymbol{\sigma}^{(2)}(\mathbf{q} = 0, \omega)$ in the long-wavelength approximation, or optical processes such as photon drag[37] and spatially dispersive photogalvanic effects[38], which are described by the first order in **q**, $\boldsymbol{\sigma}^{(2)}(\mathbf{q}^{(1)}, \omega)$ conductivity tensor, but share similarities with the polariton-drag process[39,40]. Therefore, to describe V_{HC}, a generalized conductivity tensor $\boldsymbol{\sigma}^{(2)} = \boldsymbol{\sigma}^{(2)}(\mathbf{q}, \omega)$ is derived (Supplementary Note 2.3), showing a universal nonlinear optical response because of nonvertical optical transitions.

To understand the unusual **q**-dependence of Hall photovoltage in the small-angle supertwisted system, we performed numerical simulations of the derived $\sigma^{(2)}_{xxxy}(\mathbf{q} = q_x\hat{x}, \mathbf{J} = j_x\hat{x}, \mathbf{E} \times \mathbf{E} = (E_xE_y - E_yE_x)\hat{z})$ on a few different continuum models of TMD stacks (Supplementary Note 2.4). Here excitonic effects, lattice relaxation and d.c. electric field are not incorporated for computational accessibility, but without loss of generality[41] (Supplementary Notes 2.1 and 2.7). The calculations for monolayer TMD (Fig. 4d) show that $\sigma^{(2)}_{xxxy}$ is independent of q_x, as governed by D_{3h} symmetry selection rules. This validates the usually adopted long-wavelength approximation. Figure 4e shows $\sigma^{(2)}_{xxxy}$ calculated for a K-valley twisted homobilayer TMD model system[42] with a 1° twist angle and a moiré length of about 10 nm (the scaling factor is $1/\beta$, β being the twist angle), showing a linear $\sigma^{(2)}_{xxxy}$ –**q** relationship.

However, for a multilayer supertwisted system, the higher-order **q** response depends on its coherence length, that is, the larger the coherence length, the stronger the higher-order **q** response[43]. In the small twist-angle limit (device D5; Fig. 4a), the coherence length is determined by the moiré (Fig. 4f, inset) and moiré of moiré lengthscales (>100 nm), with the latter approaching optical wavelengths (Supplementary Note 2.5). In the large twist-angle case (Fig. 4b), there is no coherence beyond the crystalline lattice scale (around 1 nm), and the moiré modulation analyses are no longer valid. It explains the contrasting experimental results observed in the two samples. To further understand the observation on device D5 in the small-angle limit, $\sigma^{(2)}_{xxxy}$ was calculated for a supertwisted TMD[41] model with a 2° twist angle (in Fig. 4f, orange dotted line is a fit with different orders in momentum **q**). The fundamental unit is a four-band trilayer TMD model[42] coupled to the neighbouring layers in the top–bottom block, which allows us to perform a Fourier expansion along the *z*-direction and define a smaller Brillouin zone. We average over the wavevector along the z-direction, k_z, which shows very prominent collective contributions from higher-order **q** terms (Fig. 4f), consistent with experiments.

Discussion

In our nonlinear response function (Supplementary Note 2.3), a smaller twist-angle enhances the interband response from momentum correlation of the Bloch wavefunctions ($\mathbf{k}$ and $\mathbf{k}+\mathbf{q}$; Fig. 4f) in the moiré of moiré bands[44]. Specifically, $\boldsymbol{\sigma}^{(2)}$ is related to $\tilde{\mathbf{v}}_{\mathbf{k}\mathbf{k}'nm}=\frac{1}{2}\langle u_{n,\mathbf{k}}|\{\mathbf{v}, e^{i\mathbf{q}\cdot\mathbf{r}}\}|u_{m,\mathbf{k}'}\rangle$, the generalized velocity operator between two Bloch states at $\mathbf{k}$ and $\mathbf{k}'$. As $\tilde{\mathbf{v}}_{\mathbf{k}+\mathbf{q}nm}$ is evaluated between two closely spaced momenta $\mathbf{k}$ and $\mathbf{k}+\mathbf{q}$, the cross product of $\tilde{\mathbf{v}}_{\mathbf{k}\mathbf{k}'nm}$ in the response function is related to the band-resolved Berry curvature, $\Omega^{i}_{nm}(\mathbf{k})$, which can be expanded as its multipoles (schematics in Fig. 4d–f). Therefore, the opto-twistronic Hall effect is a process involving higher-order quantum geometric quantities, among other intrinsic and extrinsic terms (details in Supplementary Note 2) that contribute to multipolar excitation processes assisted by $\mathbf{q}$ (such as the case of shrunken light in plasmonics[45]). Although the lowest order band geometrical tensor[16] has featured a wide range of quantum phenomena, including QAHE[46] (Fig. 4g), quantized circular photogalvanic effect[47] and nonlinear Hall effect[48–50] (Fig. 4h), the opto-twistronic Hall effect (Fig. 4i) is beyond this framework. Although a microscopic description of opto-twistronic Hall effect, especially the role of the third spatial dimension awaits further exploration, this phenomenon provides a route to study the interplay of quantum geometry, topology and correlations in complex moiré systems.

In conclusion, our study uncovers modified light–matter interactions within a 3D supertwisted WS_2 system. The twisted spiral geometry gives rise to an opto-twistronic Hall effect, determined by the handedness of the twisted layers and helicity of light. When the coherence lengthscale from moiré modulations approaches the scale of optical wavelengths, a strong alteration of the response to photon momentum is observed. The role of higher-order quantum geometric quantities on the observed photon momentum-dependent response is discussed. Moreover, the supertwisted system bridges 2D and 3D twistronics, overcoming lengthscale differences between electrons and photons to enhance optical nonlinearities beyond simple optical selection rules and pushes the boundaries of light-induced quantum phenomena.

Online content

Any methods, additional references, Nature Portfolio reporting summaries, source data, extended data, supplementary information, acknowledgements, peer review information; details of author contributions and competing interests; and statements of data and code availability are available at https://doi.org/10.1038/s41586-024-07949-1.

1. Andrei, E. Y. et al. The marvels of moiré materials. *Nat. Rev. Mater.* **6**, 201–206 (2021).
2. Sanchez-Valencia, J. R. et al. Controlled synthesis of single-chirality carbon nanotubes. *Nature* **512**, 61–64 (2014).
3. Kennes, D. M. et al. Moiré heterostructures as a condensed-matter quantum simulator. *Nat. Phys.* **17**, 155–163 (2021).
4. Cao, Y. et al. Unconventional superconductivity in magic-angle graphene superlattices. *Nature* **556**, 43–50 (2018).
5. Regan, E. C. et al. Emerging exciton physics in transition metal dichalcogenide heterobilayers. *Nat. Rev. Mater.* **7**, 778–795 (2022).
6. Wang, X. et al. Light-induced ferromagnetism in moiré superlattices. *Nature* **604**, 468–473 (2022).
7. Li, T. et al. Quantum anomalous Hall effect from intertwined moiré bands. *Nature* **600**, 641–646 (2021).
8. Xu, Y. et al. A tunable bilayer Hubbard model in twisted WSe2. *Nat. Nanotechnol.* **17**, 934–939 (2022).
9. Ma, C. et al. Intelligent infrared sensing enabled by tunable moiré quantum geometry. *Nature* **604**, 266–272 (2022).
10. Zhang, L. et al. Van der Waals heterostructure polaritons with moiré-induced nonlinearity. *Nature* **591**, 61–65 (2021).
11. Zhu, Z., Carr, S., Massatt, D., Luskin, M. & Kaxiras, E. Twisted trilayer graphene: a precisely tunable platform for correlated electrons. *Phys. Rev. Lett.* **125**, 116404 (2020).
12. Wu, F., Zhang, R.-X. & Sarma, S. D. Three-dimensional topological twistronics. *Phys. Rev. Res.* **2**, 022010 (2020).
13. Wang, Y.-Q., Morimoto, T. & Moore, J. E. Optical rotation in thin chiral/twisted materials and the gyrotropic magnetic effect. *Phys. Rev. B* **101**, 174419 (2020).
14. Crosse, J. & Moon, P. Quasicrystalline electronic states in twisted bilayers and the effects of interlayer and sublattice symmetries. *Phys. Rev. B* **103**, 045408 (2021).
15. Lian, Z. et al. Exciton superposition across moiré states in a semiconducting moiré superlattice. *Nat. Commun.* **14**, 5042 (2023).
16. Wang, N. et al. Quantum-metric-induced nonlinear transport in a topological antiferromagnet. *Nature* **621**, 487–492 (2023).
17. Liu, Y. et al. Helical van der Waals crystals with discretized Eshelby twist. *Nature* **570**, 358–362 (2019).
18. Zhao, Y. et al. Supertwisted spirals of layered materials enabled by growth on non-Euclidean surfaces. *Science* **370**, 442–445 (2020).
19. Ci, P. et al. Breaking rotational symmetry in supertwisted WS_2 spirals via moiré magnification of intrinsic heterostrain. *Nano Lett.* **22**, 9027–9035 (2022).
20. Fan, X. et al. Mechanism of extreme optical nonlinearities in spiral WS_2 above the bandgap. *Nano Lett.* **20**, 2667–2673 (2020).
21. Shearer, M. J. et al. Complex and noncentrosymmetric stacking of layered metal dichalcogenide materials created by screw dislocations. *J. Am. Chem. Soc.* **139**, 3496–3504 (2017).
22. Plechinger, G. et al. Identification of excitons, trions and biexcitons in single-layer WS_2. *Phys. Status Solidi Rapid Res. Lett.* **9**, 457–461 (2015).
23. Poshakinskiy, A. V., Kazanov, D. R., Shubina, T. V. & Tarasenko, S. A. Optical activity in chiral stacks of 2D semiconductors. *Nanophotonics* **7**, 753–762 (2018).
24. Gao, Y., Zhang, Y. & Xiao, D. Tunable layer circular photogalvanic effect in twisted bilayers. *Phys. Rev. Lett.* **124**, 077401 (2020).
25. Shen, P.-C. et al. Ultralow contact resistance between semimetal and monolayer semiconductors. *Nature* **593**, 211–217 (2021).
26. Handa, T. et al. Spontaneous exciton dissociation in transition metal dichalcogenide monolayers. *Sci. Adv.* **10**, eadj4060 (2024).
27. Mak, K. F., McGill, K. L., Park, J. & McEuen, P. L. The valley Hall effect in MoS_2 transistors. *Science* **344**, 1489–1492 (2014).
28. Kim, C.-J. et al. Chiral atomically thin films. *Nat. Nanotechnol.* **11**, 520–524 (2016).
29. Ochoa, H. & Asenjo-Garcia, A. Flat bands and chiral optical response of moiré insulators. *Phys. Rev. Lett.* **125**, 037402 (2020).
30. Stauber, T., Low, T. & Gómez-Santos, G. Chiral response of twisted bilayer graphene. *Phys. Rev. Lett.* **120**, 046801 (2018).
31. Nguyen D. X. & Son D. T. Electrodynamics of thin sheets of twisted material. Preprint at arxiv.org/abs/2008.02812 (2020).
32. Lee, J., Mak, K. F. & Shan, J. Electrical control of the valley Hall effect in bilayer MoS_2 transistors. *Nat. Nanotechnol.* **11**, 421–425 (2016).
33. Quereda, J. et al. Symmetry regimes for circular photocurrents in monolayer $MoSe_2$. *Nat. Commun.* **9**, 3346 (2018).
34. Liu, W. et al. Generation of helical topological exciton-polaritons. *Science* **370**, 600–604 (2020).
35. Munkhbat, B. et al. Self-hybridized exciton-polaritons in multilayers of transition metal dichalcogenides for efficient light absorption. *ACS Photonics* **6**, 139–147 (2018).
36. Ganichev, S. D. & Prettl, W. Spin photocurrents in quantum wells. *J. Phys. Condens. Matter* **15**, R935 (2003).
37. Glazov, M. & Golub, L. Valley Hall effect caused by the phonon and photon drag. *Phys. Rev. B* **102**, 155302 (2020).
38. Ji, Z. et al. Spatially dispersive circular photogalvanic effect in a Weyl semimetal. *Nat. Mater.* **18**, 955–962 (2019).
39. Xiong, Y., Shi, L.-k & Song, J. C. W. Polariton drag enabled quantum geometric photocurrents in high-symmetry materials. *Phys. Rev. B* **106**, 205423 (2022).
40. Shi, L.-k, Zhang, D., Chang, K. & Song, J. C. W. Geometric photon-drag effect and nonlinear shift current in centrosymmetric crystals. *Phys. Rev. Lett.* **126**, 197402 (2021).
41. Zhu, Z., Cazeaux, P., Luskin, M. & Kaxiras, E. Modeling mechanical relaxation in incommensurate trilayer van der Waals heterostructures. *Phys. Rev. B* **101**, 224107 (2020).
42. Wu, F., Lovorn, T., Tutuc, E., Martin, I. & MacDonald, A. Topological insulators in twisted transition metal dichalcogenide homobilayers. *Phys. Rev. Lett.* **122**, 086402 (2019).
43. Gassner, S. & Mele, E. J. Regularized lattice theory for spatially dispersive nonlinear optical conductivities. *Phys. Rev. B* **108**, 085403 (2023).
44. Chaudhary, S., Lewandowski, C. & Refael, G. Shift-current response as a probe of quantum geometry and electron-electron interactions in twisted bilayer graphene. *Phys. Rev. Res.* **4**, 013164 (2022).
45. Koenderink, A. F., Alù, A. & Polman, A. Nanophotonics: shrinking light-based technology. *Science* **348**, 516–521 (2015).
46. Nagaosa, N., Sinova, J., Onoda, S., MacDonald, A. H. & Ong, N. P. Anomalous Hall effect. *Rev. Mod. Phys.* **82**, 1539–1592 (2010).
47. de Juan, F., Grushin, A. G., Morimoto, T. & Moore, J. E. Quantized circular photogalvanic effect in Weyl semimetals. *Nat. Commun.* **8**, 15995 (2017).
48. Ma, Q. et al. Observation of the nonlinear Hall effect under time-reversal-symmetric conditions. *Nature* **565**, 337–342 (2019).
49. Sodemann, I. & Fu, L. Quantum nonlinear Hall effect induced by Berry curvature dipole in time-reversal invariant materials. *Phys. Rev. Lett.* **115**, 216806 (2015).
50. Ma, Q., Grushin, A. G. & Burch, K. S. Topology and geometry under the nonlinear electromagnetic spotlight. *Nat. Mater.* **20**, 1601–1614 (2021).

Methods

Sample growth

The supertwisted WS_2 structures were synthesized following previous reports[18,21,51]. WO_3 nanoparticles (Sigma Aldrich, nanopowder <100 nm particle size) dispersed in ethanol were drop-cast onto a 300-nm SiO_2/Si substrate and dried before the reaction. WS_2 precursor powder (100 mg, Alfa Aesar) in an alumina boat was placed in the first zone of a three-zone furnace. The substrates were placed between the second and the third zone with the polished side facing up. $CaSO_4{\cdot}2H_2O$ powder (1 g; Sigma Aldrich) was placed upstream from the heating zone as the water vapour source and heated with heating tapes. With 100 sccm argon flowing at 800 torr, the second zone was heated to 1,200 °C at a rate of 20 °C min^{-1}, and simultaneously the third zone was heated to 700 °C at the same rate, whereas the $CaSO_4{\cdot}2H_2O$ was not heated. Once the furnace temperatures were reached, the $CaSO_4{\cdot}2H_2O$ was heated to 90 °C to release the water vapour. After all the temperatures were stabilized, the WS_2 boat was pushed into the second zone by a magnet-coupled positioner and a quartz rod to initiate the reaction. After 15 min reaction, the furnace was opened and cooled down rapidly[18].

Device fabrication

Hall bar devices of the supertwisted flakes were geometrically defined by electron beam lithography (EBL) followed by CH_3F/O_2 plasma reactive ion etching for 60 s. The protection layer is PMMA A8 495. Electrodes are further patterned by EBL, followed by metal deposition by physical vapour deposition processes. Electrodes consist of 40 nm bismuth and a 35–100 nm copper/gold capping layer, depending on the thickness of supertwisted samples.

Angle-resolved reflectance measurements

The measurements were carried out in a custom-built angle-resolved microscopy system coupled to a cryostat (Janis Research, ST-500). The sample was excited by a white light beam focused by an objective (60X, 0.7NA, Nikon) and the reflected light was collected by the same objective, with its back focal plane imaged onto the entrance slit of a spectrometer (Acton SpectraPro 500i). The spectrometer CCD recorded both the wavelength of light and its spatial position at the entrance slit (angles of the reflected light) to extract the angle- and wavelength-resolved reflectance spectrum.

Opto-twistronic Hall effect measurement

Hall effect measurements were carried out in the same cryostat (Janis Research, ST-500) (refs. 52,53). The sample was excited by a continuous wavelength tunable (400–2,400 nm) supercontinuum laser (NKT Photonics) beam, focused by an objective (60X, 0.7NA, Nikon). The incidence angle was controlled by a retroreflector operated on a motorized stage and the exact angle is identified by a Fourier plane imaging of the beam. Transverse voltage was applied by a Keithley 2400 sourcemeter. The supermonochromatic quarter-wave plate after the polarizer was rotated at the frequency of 200–300 Hz, and the signals at its second and fourth harmonics were recorded with a SR860 lock-in amplifier. As in a full 360-degree rotation of a quarter-wave plate, there are two periods of change in circular polarization, and four periods of changing in linear polarization (Fig. 2c), the photovoltage signals recorded at the second and fourth harmonics correspond to the parts sensitive to circular (for example, V_{HC}) and linearly polarized modulations (for example, V_{HL}), respectively (Extended Data Fig. 2).

Model description of the opto-twistronic Hall effect

To describe the opto-twistronic Hall phenomena in the supertwisted system, we model the light field as $E_i(\mathbf{r}, t) = E_i^{i(\mathbf{q}\cdot\mathbf{r}-\omega t)} + \text{c. c.}$ where $\mathbf{q}$ and ω span the momentum and frequency spaces. The Hall current dependent on circular polarization, $\mathbf{J}(\mathbf{q}, \omega)$, is determined by a nonlinear conductivity tensor $\boldsymbol{\sigma}^{(2)}$ and $(\mathbf{E}\times\mathbf{E}^*)$, the pseudo-vector depicting light helicity. $\boldsymbol{\sigma}^{(2)}$ is a material-dependent, complex function in the $(\omega, \mathbf{q})$ space. Carrier dynamics in the supertwisted material can be analysed by considering the free propagation of a particle in a helical frame of reference. A free-particle Hamiltonian quadratic in momentum, $H = \mathbf{p}\cdot\frac{\mathbf{p}}{2m}$ in the co-rotating frame of the crystal is augmented by a geometric connection as seen in the lab frame, leading to a quasi-momentum operator, $\hbar\kappa_z = p_z + \hbar\beta\hat{m}_z$, where $\beta = \frac{d\phi}{dz}$ is the pitch of the helix and $\hat{m}_z = xp_y - yp_x$ is the z-component of the orbital angular momentum. κ_z is the generator for the nonsymmorphic screw symmetry operation of the stack and its eigenvalues play the part of conserved Bloch momenta for interlayer translations coupled to rotations. Completing the squares in H gives the transformed Hamiltonian (Supplementary Note 2.2),

$$H = \frac{1}{2m}[(p_x + \hbar\kappa_z\beta y)^2 + (p_y - \hbar\kappa_z\beta x)^2 + (\hbar\kappa_z)^2(1-\beta^2(x^2+y^2)) + (\hbar\beta\hat{m}_z)^2] \quad (1)$$

with transformed momenta $\Pi_x = p_x + \hbar\kappa_z\beta y$ and $\Pi_y = p_y - \hbar\kappa_z\beta x$ that obey the commutation relation $[\Pi_x, \Pi_y] = 2i\hbar^2\kappa_z\beta$. Thus, in each sector with fixed κ_z, the in-plane differential translations do not commute, analogous to the situation for a particle with charge e moving in a uniform magnetic field with strength $B^* = 2\hbar\kappa_z\beta/e$. However, unlike the situation for a physical magnetic field, here the effective field B^* is odd in the quasi-momentum κ_z, reflecting the fact that the twisted structure preserves the time-reversal symmetry. Any nonequilibrium state distribution that breaks time-reversal symmetry, for example, under excitation with circularly polarized light, will undergo a net transverse deflection in response to an applied in-plane bias and can be identified by the induced Hall response. Importantly, the field responsible for this deflection B^* is also odd in β, so that the sign of the Hall field is reversed in enantiomeric structures, as observed. Without considering external excitation, the effective field B^* is now a purely geometrical quantity, originating from its non-commutative property and specified by the degree of twist and the conserved value of κ_z.

Data availability

The data in the main figures are provided with this paper. Other data that support the findings of this study are available from the corresponding authors upon reasonable request. Source data are provided with this paper.

Code availability

Codes that support the findings of this study are available from the corresponding authors upon reasonable request.

51. Zhao, Y. & Jin, S. Stacking and twisting of layered materials enabled by screw dislocations and non-Euclidean surfaces. *Acc. Mater. Res.* **3**, 369–378 (2022).
52. Ji, Z. et al. Photocurrent detection of the orbital angular momentum of light. *Science* **368**, 763–767 (2020).
53. Dhara, S., Mele, E. J. & Agarwal, R. Voltage-tunable circular photogalvanic effect in silicon nanowires. *Science* **349**, 726–729 (2015).

Acknowledgements We thank X. Fan for the discussions. This work was supported by the US Air Force Office of Scientific Research (award no. FA9550-20-1-0345) and by the NSF-DMREF grant to R.A. (NSF-2323468) and S.J. (NSF-2323470). This work is also supported by NSF-2230240 and NSF-QII-TAQS-#1936276. The polariton studies were supported by the Office of Naval Research (grant no. N00014-22-1-2378). This work was also partially supported by a seed grant from the Center for Precision Engineering for Health (CPE4H) at the University of Pennsylvania. Numerical calculations were supported by a seed grant from the University of Pennsylvania Materials Research Science and Engineering Center (MRSEC) (NSF DMR-1720530). Device fabrication and characterization work was supported by the King Abdullah University of Science and Technology (OSR-2020-CRG9-4374.3) and was carried out at the Singh Center for Nanotechnology, which is supported by the NSF National Nanotechnology Coordinated Infrastructure Program under grant no. NNCI-1542153. Work by E.J.M. is

supported by the Department of Energy under grant no. DE-FG02-84ER45118. Z.J. and Z.Z. acknowledge support from the Stanford Science fellowship.

Author contributions E.J.M. and Z.J. developed the theoretical model of generalized nonlinear conductivity. Z.J. and R.A. designed the experiments. Z.J. fabricated devices, and Z.J. and Y.C. performed optical Hall measurements. Y.Z. synthesized the material under the supervision of S.J.; Y.W. and Z.J. performed reflectance measurements. W.L. conducted polariton simulations. Z.Z. and E.J.M. developed theoretical models and performed numerical calculations. Y.Z., Z.J. and G.M. carried out the AFM measurements. R.A. supervised the project. Z.J., Z.Z., W.L., E.J.M. and R.A. wrote the paper with input from all authors.

Competing interests The authors declare no competing interests.

Additional information

Supplementary information The online version contains supplementary material available at https://doi.org/10.1038/s41586-024-07949-1.

Correspondence and requests for materials should be addressed to Ritesh Agarwal.

Peer review information *Nature* thanks Ioannis Paradisanos and the other, anonymous, reviewer(s) for their contribution to the peer review of this work. Peer reviewer reports are available.

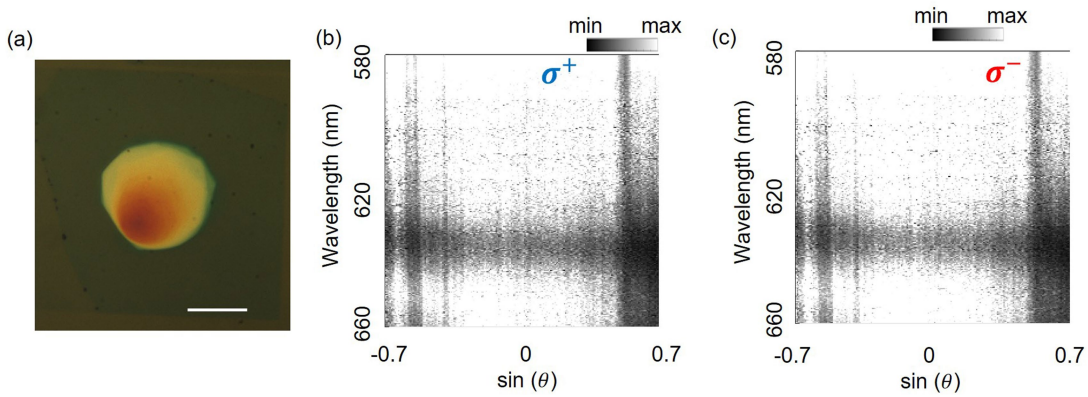

Extended Data Fig. 1 | Details of the linear optical measurement. a, Optical image of the supertwisted WS_2 sample, scale bar: 5 μm. **b-c**, The angle resolved reflectance spectra measured with left and right circularly polarized light, respectively. The colour plot shows the value of the differential reflectance $(R - R_0)/R_0$ (R_0 measured on the substrate, R measured on the sample). Figure 1c is the line plot averaged over 70 incidence angles.

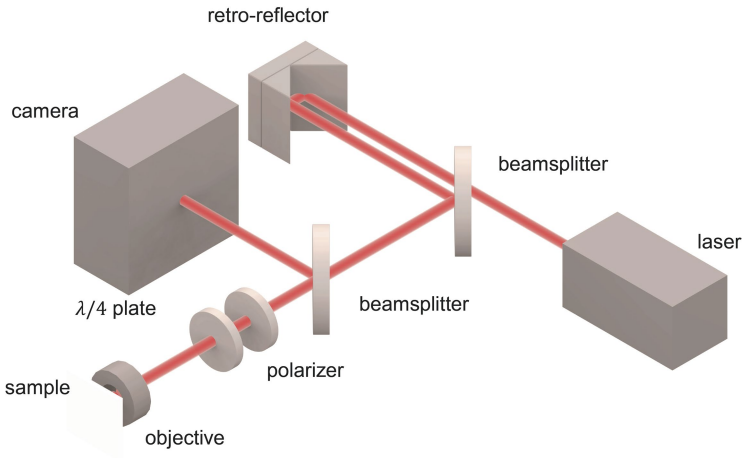

Extended Data Fig. 2 | A schematic of the experimental setup for opto-twistronic Hall effect measurements. The retroflector controls the laser incidence angle, and the quarter wave plate controls the polarization of light.